2-13-2023

Effects of intermixing and oxygen vacancies on a two-dimensional electron gas at the polar ($TbScO_3$/KTaO) (001) interface

Bhubnesh Lama

Evgeny Y. Tsymbal

Tula R. Paudel

Effects of intermixing and oxygen vacancies on a two-dimensional electron gas at the polar ($TbScO_3/KTaO_3$) (001) interface

Bhubnesh Lama,[1] Evgeny Y. Tsymbal,[2] and Tula R. Paudel[1,2,*]

[1]*Department of Physics, South Dakota School of Mines and Technology, Rapid City, South Dakota 57701, USA*

[2]*Department of Physics and Astronomy & Nebraska Center for Materials and Nanoscience, University of Nebraska, Lincoln, Nebraska 68588, USA*

(Received 10 November 2022; accepted 26 January 2023; published 13 February 2023)

3*d*-5*d* perovskite oxides, ABO_3 (where *A* and *B* are 3*d* or 5*d* elements), form polar surfaces in the (001)-stacked thin films. As a result, the polar-polar (001) interface between two ABO_3 insulators could create polar discontinuity potentially producing a two-dimensional electron gas of higher density and stronger spatial localization compared to the widely studied polar-nonpolar oxide interfaces, such as (001) $LaAlO_3/SrTiO_3$. Here, as a model system, we explore the interface between polar (001) $TbScO_3$ and polar (001) $KTaO_3$ using first-principles density functional theory. We find that the intermixed interface $Ta_{0.75}Sc_{0.25}O_2/Tb_{0.75}K_{0.25}O$ maintaining the bulk perovskite charge stacking (e.g., $\ldots + 1/ - 1/ + 1 \ldots$) is insulating and has a lower energy than the metallic interface TbO/TaO_2 breaking such stacking. This intermixed interface is, however, prone to the formation of oxygen vacancies which make it conducting. We emphasize that the driving force for the formation of the two-dimensional electron gas (2DEG) here is not a built-in electric field stemming from the polar discontinuity but the interface stoichiometry. We find that the ratio of oxygen vacancy concentration is a factor of 30 times larger at the interface than in bulk KTO at room temperature. The oxygen vacancy-induced 2DEG resides on the Ta-5*d* electronic orbitals with d_{xy} and $d_{xz/yz}$ occupation dominating overall charge density near and far away from the interface.

DOI: 10.1103/PhysRevMaterials.7.026201

I. INTRODUCTION

Interfaces between two insulating materials can be nonpolar or polar. In the latter case, an abrupt change in the ionic charge sequence across the interface produces polar discontinuity that generates an energetically unfavorable electric field. The mechanism that eliminates (reduces) this polar discontinuity determines the electronic nature of the interface. The compensation of the interface-bound charge via a free charge transfer yields interface metallicity. The famous example is the formation of a two-dimensional electron gas (2DEG) at the $LaAlO_3$(LAO)/$SrTiO_3$(STO) interface oriented normal to the (001) direction [1]. The polar catastrophe model [2], commonly used to describe its formation, predicts that the polar discontinuity at the interface is compensated by electron transfer from the valence band of the $LaAlO_3$ surface layer making the interface conducting [1,3]. This model successfully explains the critical thickness above which the interface becomes conducting and predicts that the interfacial charge density increases slowly with the thickness and converges to 0.5e/uc in the limit of infinite thickness. Other mechanisms used to explain the 2DEG formation at the interfaces include intermixing [2,4,5] to create donor-type defects, e.g., La_{Sr} antisites, oxygen vacancies [6–12], and surface protonation redox reactions [13,14].

Alternatively, the polar discontinuity across an interface between two insulating materials may be removed via cation intermixing and nonstoichiometry, rendering the interface insulating. This fact is less appreciated in the literature but prevalent in many, including 3d-5d polar-polar oxides heterostructures. At the interface involving $A^{+1}B^{+5}O_3$ and $A\prime^{+3}B\prime^{+3}O_3$, the charge discontinuity is twice as large as that at the LAO/STO (001) interface, e.g., $(TaO_2)^{+1}/(TbO)^{+1}$ stacking in $TbScO_3/KTaO_3$.

Such a large charge discontinuity could either drive electron transfer and render the interface metallic or induce the interfacial intermixing or nonstoichiometry and render the interface insulating. The cation intermixing has been earlier suggested to mitigate polar catastrophe in semiconductors polar heterostructures [15–17] yielding to charge neutral interfaces. The intermixing plays a major role in superlattices interfaces and heterostructures with the compensated surface. Note that, in these compounds, another stacking possibility that maintains charge continuity, $(TaO_2)^{+1}/(ScO_2)^{-1}$ breaks natural $AO/B'O_2$ or $AO_2/B'O$ stacking of perovskite structure and stoichiometry usually unstable.

Experimentally out of the interfaces that maintain perovskite stacking, some (epitaxial unless specified) are metallic such as (111)-oriented $LaAlO_3/KTaO_3$ [18], amorphous $LaAlO_3$ on (001)−oriented $KTaO_3$ film [19], $LaVO_3/KTaO_3$ [20,21], and $LaTiO_3/KTaO_3$ [22,23], $LaCrO_3/KTaO_3$ [24], (111)−oriented $LaAlO_3/SrTiO_3$ [25], while the others, $GdScO_3/KTaO_3$ [26] and $LaScO_3/KTaO_3$ [27], are insulating. These raise the possibility that at some interfaces, compensation of the polar discontinuity by an interfacial electron gas is energetically more favorable, while at others, the polar discontinuity leads to intermixing. For the latter interfaces, however, oxygen vacancies still may lead to the

*Corresponding author: tula.paudel@sdsmt.edu

interfacial 2DEG. Incidentally, the reported metallic interfaces are all grown at low oxygen partial pressure <1 mTorr, or in the presence of reducing agents such as H [18], while the insulating interfaces are grown at relatively high pressure (0.1 Torr), boosting the theory that relies on the possibility of oxygen vacancy induced 2DEG in these interfaces. Additionally, the measured 2DEG density, though it varies upon growth conditions and material systems, is generally lower $\sim 10^{12}$–$10^{13}\,\mathrm{cm}^{-2}$ compared to the theoretical prediction of $5\times10^{14}\,\mathrm{cm}^{-2}$ based on the polar catastrophe model.

In this work, we investigate the interplay between cation intermixing, oxygen vacancies, and the interfacial conductivity in the prototypical (001) interface of polar oxide $TbScO_3$ (TSO) and $KTaO_3$ (KTO) by using the first-principles density functional theory. We intermix the cations at the interface in all possible ways to annihilate charge discontinuity and calculate their grand potentials. We find that the intermixed interface $(K_{0.25}Tb_{0.75}O)^{+0.5}/(Ta_{0.75}Sc_{0.25}O_2)^{+0.5}$ has the lowest grand potential, lower than that of the nonmixed interface, indicating that the intermixed interface is the most stable. We find that the intermixed interface is insulating; however, upon introducing oxygen vacancies, the interface becomes conducting. The behavior of oxygen vacancies at these interfaces is very different from the behavior of those in bulk KTO, where they form a localized nonconducting band in the middle of band gap [28]. The predicted behavior of the defect-induced 2DEG at the TSO/KTO interface can be also expected at other polar-polar oxide interfaces.

II. COMPUTATIONAL METHODS

We use density functional theory implemented in Vienna *ab-initio* Simulation Package (VASP) within the plane-wave pseudopotential method [29,30]. The projected augmented wave [31] method is used to approximate the electron-ion potential, and the Perdew-Burke-Ernzerhof (form of the generalized gradient approximation (GGA) [32] is used to approximate exchange-correlation effects. The Ta and Tb pseudopotentials include $5p^6\,6s^2\,5d$ and $5p^6 6s$, as respectively, as valence state while *4f* orbitals are included in pseudopotential core. The pseudopotentials of K, Sc and O include $3s^2 3p^6 4s$, $3p^6 4s^2 3d$ and $2s^2 2p$ as valence orbitals. The heterostructure calculations are performed by using a kinetic energy cutoff of 340 eV, *k*-point mesh of $5\times5\times1$ and convergence criteria for the energy difference of 10^{-5} eV and the atomic force of $0.05\,\mathrm{eV\,Å^{-1}}$. We have ignored effects of spin-orbit coupling in the calculations. The bulk Born effective charges and dielectric constants are calculated with the same kinetic energy cutoff and other computational parameters except for the *k* points of $7\times7\times7$ for KTO and $5\times5\times4$ for TSO. We use the density functional perturbation theory [33,34] as implemented in VASP for computations of the Born effective charges and dielectric constants (Supplemental Material [35] S6, and references therein [36–41]).

III. RESULTS AND DISCUSSION

A. Bulk $KTaO_3$ and $TbScO_3$

The $KTaO_3$ (KTO) is a common substrate like $SrTiO_3$ (STO) and behaves similarly to a large extent. KTO is also a paraelectric material with a band gap ~3.5 eV [42,43] and lattice constants 3.99 Å that crystallizes in a simple cubic lattice [Fig. 1(a)] with space group 225 (*Pm*3*m*). The sizeable spin-orbit coupling (SOC) is a notable difference in KTO compared to STO. As a result, the lowest conduction band splits by about 400 meV into a lower $J = 3/2$ doubly degenerate band containing light and heavy electrons and an upper $J = 1/2$ SOC split band. The presence of large SOC in KTO drives number of spin-related phenomena including weak antilocalization [44] and Rashba spin splitting [45,46].

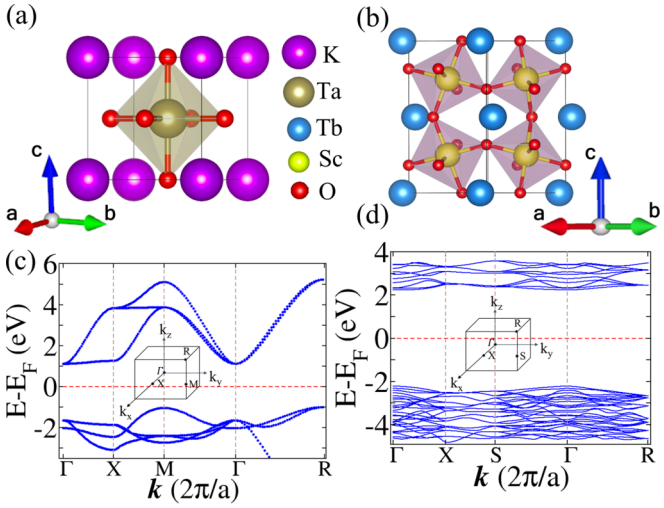

FIG. 1. Crystal structures of bulk cubic $KTaO_3$ (a), orthorhombic $TbScO_3$ (b), and their corresponding band structures (c) and (d). Inset in (c) and (d) shows the corresponding Brillouin zones. Zero of the energy scales corresponds to the Fermi level. The vertical dashed lines indicate high symmetry points in the Brillouin zones.

$TbScO_3$ (TSO), on the other hand, crystallizes in $GdFeO_3$ type orthorhombic structure with space group 62 (*Pnma*), as shown in Fig. 1(b). The large deviation of the Goldschmidt structural factor, 0.78, from the ideal value, 1, leads to stabilization of the distorted Pnma phase. Because of reduced structural symmetry, the conduction band minimum (CBM) is nondegenerate in TSO, and the effect of SOC is not as dramatic as in KTO.

Our calculations indicate a slight lattice mismatch and the possibility of a good epitaxy between TSO and KTO. We find that the KTO lattice constant of 4.02 Å is close to the pseudocubic lattice constant, 3.86 Å, of TSO. The orthorhombic lattice constants are a = 5.47 Å, b = 5.76 Å, and c = 8.0 Å. The GGA approximation used in the calculation is known slightly overestimate the lattice constants up to a few percent, and underestimate the electronic band gap due to spurious self-interaction [47].

The calculated electronic band structure of KTO [Fig. 1(c)] shows an indirect band gap of 2.0 eV with the valence band maximum (VBM) at the R point and the CBM at the Γ point of the Brillouin zone, consistent with the previous calculations [48]. Similarly, the electronic band structure of TSO [Fig. 1(d)] shows a direct band gap of 4.2 eV with both VBM and CBM at the Γ point. Oxygen-p bands dominate the VBM of both compounds. In contrast, the CBM is dominated by the degenerate d_{xy}, d_{yz}, and d_{xz} bands corresponding to

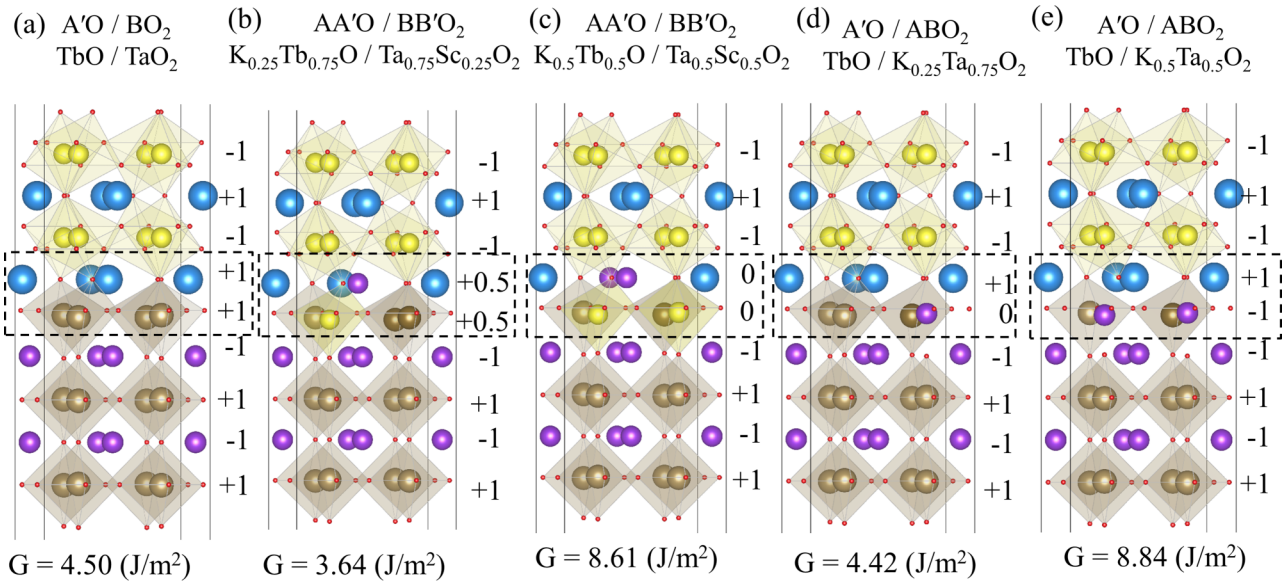

FIG. 2. Different configurations of TSO/KTO heterostructures and possible ways of intermixing the cations at the interface (the marking at the top of each structure) and their calculated grand potential energy G (the marking at the bottom structure). The dashed black rectangle in each heterostructure denotes the heterointerface. The numbers at the side of each structure represent the ionic charge value at each layer.

crystal-field split t_{2g} bands of Ta-5d electronic orbitals in KTO. In TSO, however, the CBM consists of nondegenerate $d_{x^2-y^2}$ and d_{yz} bands of Sc-3d electronic orbitals because of directional crystal field in orthorhombic compound with different lattice constants, b > c > a.

For the 2DEG to reside in KTO, it is necessary that the band gap of KTO is smaller than that of TSO. Our calculations, like experiments, show that this condition is satisfied. The calculated band gap of TSO, 3.6 eV, is much larger than that of KTO, 2.0 eV, similar to the experiments: TSO band gap, ∼6.1 eV [49] is larger than KTO band gap, ∼3.5 eV [42,43].

B. TSO/KTO (001) heterostructure (HS)

1. Interfacial structure

To understand the atomic configuration of the interfaces, we consider $(TSO)_{5.5}/(KTO)_{3.5}$ (001) superlattices with supercells shown in Fig. 2. For lattice matching and reducing interfacial strain between TSO and KTO, we use $\sqrt{2}\times\sqrt{2}$ supercell of cubic KTO. Resulting strain in the TSO overlayer is relatively small, $\sim -3.8\%$ (compressive) along the a axis and $+1.2\%$ (tensile) along the b axis. The KTO slab is chosen to be nonstoichiometric (terminated by TaO_2 on both sides) to eliminate spurious electric fields that would otherwise introduce band bending in KTO.

As both KO and TaO_2 layers in KTO and TbO and ScO_2 layers in TSO have nonzero ionic charges, the KTO/TSO interface with pristine TbO/TaO_2 and KO/ScO_2 interfaces have interfacial charges of 2e/uc and −2e/uc, respectively, where uc denotes pseudocubic unit cell. Such a large interfacial charge may drive ionic intermixing to reduce the charge accumulation and hence the energy of the system.

To explicitly explore this possibility, we consider KTO/TSO interfaces with various compositions: (a) a pristine TbO/TaO_2 layer sequence [Fig. 2(a)] with interfacial charge stacking of $-1(+1|+1)-1$; here the parentheses, (), represents charge corresponding to the interfacial bilayers and intermixed interfaces, (b) $K_{0.25}Tb_{0.75}O/Ta_{0.75}Sc_{0.25}O_2$ with interfacial charge stacking of $-1/(+0.5|+0.5)/-1$ [Fig. 2(b)], (c) $K_{0.5}Tb_{0.5}O/Ta_{0.5}Sc_{0.5}O_2$ with interfacial charge stacking of $-1/(0|0)/-1$ [Fig. 2(c)], (d) $(TbO)^{+1}/(K_{0.25}Ta_{0.75}O_2)^0$ with interfacial charge stacking of $-1/(+1)/-1$ [Fig. 2(d)], and finally (e) $(TbO)^{+1}/(K_{0.5}Ta_{0.5}O_2)^{-1}$ with interfacial charge stacking of $-1(+1/-1)-1$ [Fig. 2(e)]. To determine their relative stability, we compare their grand potentials, $G = (E_s - n_1E_{TSO} - n_2E_{KTO} - n_3E_{TaO_2} \pm \sum_i m_i\,\mu_i)/A$, where, n_i represents the number of bulk TSO, KTO, and extra layer TaO_2 with corresponding energies E_{TSO}, E_{KTO} and E_{TaO_2} respectively, m_i represents the number of elements with corresponding energy, μ_i, required to maintain the particle numbers in between different trilayer stacks, and E_s represents the energy of a supercell. We find that the interface $K_{0.25}Tb_{0.75}O/Ta_{0.75}Sc_{0.25}O_2$ [Fig. 2(b)] with the interfacial charge stacking of $-1/(+0.5|+0.5)/-1$ has the lowest grand potential. This interface maintains the alternating ionic charge …/−1/(+1)/−1/… which eliminates polar discontinuity and makes the interface nonpolar.

Among the KTO/TSO interfaces that maintain charge stacking …/−1/(+1)/−1/…, we find the grand potential to be smaller when the charged layers are separated from each other, because of the reduced Coulomb repulsion. Among the two heterostructures maintaining the perovskite alternating charge stacking $-1/(+1)/-1$, the interfacial structure $(ScO_2)^{-1}/((K_{0.25}Tb_{0.75}O)^{+0.5}/(Ta_{0.75}Sc_{0.25}O_2)^{+0.5})/(KO)^{-1}$ (b) has a lower grand potential compared to $(ScO_2)^{-1}/((TbO)^{+1}/(Ta_{0.5}Sc_{0.5}O_2)^0)/(KO)^{-1}$ (d). For the former interface, the charge (total of +1) is distributed in two layers, while for the latter, charges are concentrated in the same layer.

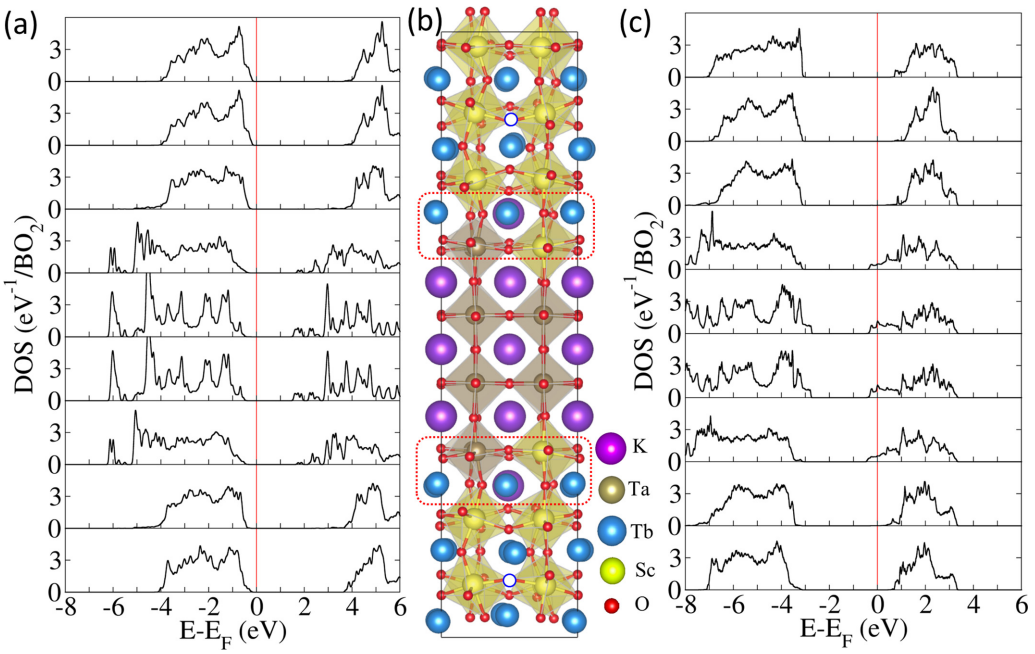

FIG. 3. Atomic structure for TSO/KTO/TSO heterostructure with $K_{0.25}Tb_{0.75}O/Ta_{0.75}Sc_{0.25}O_2$ intermixing at the interface (b). In (b) the intermixed layers are denoted by the red dotted rectangles, and white dots denotes the oxygen vacancies. The layered resolved density of states (LDOS) as a function of energy, for the heterostructure with the intermixed interface (a) and for the intermixed interface with oxygen vacancies (c). In (a) and (c) the vertical red lines represent the Fermi energy level.

Among the other interfaces that tend to accumulate a charge at the interface, we find that intermixing increases the grand potential. The grand potential of heterostructures with intermixed interfaces, i.e., $(ScO_2)^{-1}/((TbO)^{+1}/(K_{0.5}Ta_{0.5}O_2)^{-1}))/(KO)^{-1}$ (e) and $(ScO_2)^{-1}/((K_{0.5}Tb_{0.5}O)^{0}/(Ta_{0.5}Sc_{0.5}O_2)^{0})/(KO)^{-1}$ (c), is larger than the grand potential of the heterostructure with the pristine $(ScO_2)^{-1}/(TbO)^{+1}/(TaO_2)^{+1}/(KO)^{-1}$ interface (a). This suggests that the intermixing is an endothermic process except for the cases where it resolves charges discontinuity.

Unfortunately, heterostructures with small values of the grand potential lack interfacial charge discontinuity, and such heterostructures with $(ScO_2)^{-1}/((K_{0.25}Tb_{0.75}O)^{+0.5}/(Ta_{0.75}Sc_{0.25}O_2)^{+0.5})/(KO)^{-1}$ (b) and $(ScO_2)^{-1}/((TbO)^{+1}/(Ta_{0.5}Sc_{0.5}O_2)^{0})/(KO)^{-1}$ (d) interfacial structures are found to be insulating. Figure 3(a) shows layer-resolved density of states (LDOS) as a function of energy for the heterostructure with the (b) type intermixing. Each panel in the figure represents the LDOS of a ScO_2 layer in TSO or a TaO_2 layer in KTO. The Fermi energy lies in the band gap of both KTO and TSO, indicating that the system is insulating. The LDOS plot of a supercell with (d) type intermixing is shown in Fig. S1. This contrasts sharply with the pristine interface (a), which is found to be *n*-type (electron) conducting, as shown in Fig. S2. Similarly, interfaces (c) and (e) are found to be *p*-type (hole) conducting, as shown in Fig. S3 and Fig. S4, respectively. Note that interfaces (a), (c), (d), and (e) are unstable with respect to interface (b).

2. *Oxygen vacancy induced 2DEG*

Given the ubiquitous presence of oxygen vacancies in oxides, we consider a possibility of inducing 2DEG in these heterostructures by oxygen vacancies. We consider a TSO/KTO heterostructure with the $K_{0.25}Tb_{0.75}O/Ta_{0.75}Sc_{0.25}O_2$ interface that has the lowest grand potential and explore different cases where vacancy may be formed, such as (a) ScO_2 layer and (b) TbO layer on the TSO side, (c) KO layer and (d) TaO_2 layer on the KTO side, and (e) $K_{0.25}Tb_{0.75}O$ and (f) $Sc_{0.25}Ta_{0.75}O_2$ intermixed layers. To find out the likelihood of oxygen vacancy formation in all these cases, we calculate the formation energy of oxygen vacancy by using $\Delta H(V_O) = E_{SCwV_O} - E_{SCwoV_O} + \mu_O$, where, E_{SCwV_O} and E_{SCwoV_O} are the energy of superlattice with and without oxygen vacancy V_O respectively, and μ_0 is the oxygen chemical potential which is taken as $1/2E_{O2}$(molecule). We tabulate the values in Table I. Our calculated values show that oxygen vacancy formation energy is minimum when the oxygen vacancy is present at the $K_{0.25}Tb_{0.75}O$ intermixed layers. This indicates the formation

TABLE I. Calculated oxygen vacancy formation energy HF, for oxygen vacancy in bulk and different layer of the heterostructures

Oxygen position	Vacancy ΔH (eV)	
Bulk KTO	6.41	
Bulk TSO	6.77	
Heterostructure	Superlattice	Slab
ScO_2(TSO)	6.24	
TbO(TSO)	6.37	
TaO_2(KTO)	6.31	3.63
KO(KTO)	6.35	2.79
$Sc_{0.25}Ta_{0.75}O_2$ (Intermixed layer)	6.20	2.86
$K_{0.25}Tb_{0.75}O$ (Intermixed layer)	5.11	2.56

of oxygen vacancy at the interface precedes their formation anywhere else, including in KTO.

Out of different possible locations of oxygen vacancies within the $K_{0.25}Tb_{0.75}O$ layer, the oxygen vacancy located nearby the substituted site (K_{Tb}) in between two Sc atoms along [001] has the lowest energy, 5.11 eV. Other configurations of oxygen vacancies in this layer and in the other interfacial layer, $Sc_{0.25}Ta_{0.75}O_2$ have noticeably higher formation energy (>5.9 eV) (Supplemental Material [35] S2).

The $K_{0.25}Tb_{0.75}O$ layer behaves more like the TbO layer in TSO but with modified orthorhombic distortion because of local stress created by a larger K^{1+} ion with the ionic radii of 132 pm in the place of Tb^{3+} ion with the ionic radius of 92 pm [50]. The octahedral tilt in $K_{0.25}Tb_{0.75}O$ (given by Ta-O-Ta bond angle in the [001] direction) is found to be 31° compared to the tilt of 43° in TSO. Despite the significant orthorhombic distortion, lattice constants at the interface remain close to cubic $c/b \approx c/a \approx 1$ in contrast to c/b of 0.98 and c/a of 1.03 in TSO, due to its proximity with cubic KTO.

The oxygen vacancy releases the local stress at the K_{Tb} site, allowing a further increase in the octahedral tilt in $K_{0.25}Tb_{0.75}O$ along the [001] direction from 31° to 36°. Freeing up the local stress allows the system to reach its natural orthorhombic state. The defect-induced electrons move from the defect site to the nearby Ta atoms directly below and above the defect in the [001] direction, thereby reducing their ionic charges. As a result, the average Ta-O bond length along the [001] direction increases from 2.06 to 2.15 Å while the Sc-O bond length decreases to 2.06 A from 2.18 A. The resulting lattice surrounding oxygen vacancy is similar to that of TSO with c/b ∼ 1.01 and c/a ∼ 1.02.

To further prove that the substitution and orthorhombic distortion in $TbScO_3$ are responsible for the formation of oxygen vacancy in the $K_{0.25}Tb_{0.75}O$ layer, we evaluate the oxygen vacancy formation energy in the doped TbO layer of bulk TSO with $K_2Tb_2O_2$ stoichiometry. We find it to be 5.26 eV that is close to the value of the oxygen vacancy formation energy at the TSO/KTO interface (5.11 eV). We note that the formation of oxygen vacancy at the TSO/KTO interface breaks the usual perovskite stacking of $\ldots 1+/1-/1+\ldots$ and dopes the system with electrons. We choose to create an oxygen vacancy in $K_2Tb_2O_2$ layer of bulk TSO to mimic the same charge imbalance as that created by oxygen vacancy at the TSO/KTO interface.

The reduced oxygen vacancy formation energy results in a significantly larger number of oxygen vacancies at the interface than in bulk KTO or TSO. Using the expression $N(V_O) = N_A \exp(-\Delta H/k_B T)$, where N_A, k_B, and T represents the concentration of available sites, the Boltzmann constant, and temperature, respectively, for evaluation of the number of oxygen vacancies $N(V_O)$, we estimate the excess of oxygen vacancies at the interface to be $\Delta N/N = (N(V_{OI}) - N(V_{OKTO}))/N(V_{OKTO}) = \exp(-\Delta H_I + \Delta H_{KTO})/k_B T - 1$, which is ∼4150% for typical growth temperatures of 1000K. As ΔH_I is smaller than ΔH_{KTO} the exponent is positive, and hence when temperature increases, $\Delta N/N$ decreases and ranges between 8400% to 2700% for the temperature range of 500 to 1500 K.

The absolute value of the oxygen vacancy concentration, however, depends on boundary conditions and growth conditions. To illustrate the effect of the boundary conditions, we consider the same structure with vacuum next to TSO to represent the interface between finite TSO slab grown on KTO substrate. Table I shows the evaluated formation energy. Like the earlier case, the formation energy is found to be the smallest in $K_{0.25}Tb_{0.75}O$ layer, but the absolute value is much smaller, 2.56 eV, than that in the superlattice. Note that this value is likely to depend upon the slab thickness and surface termination.

The effect of growth conditions at the thermodynamic equilibrium can be estimated by using the relation between temperature, pressure, and the oxygen chemical potential, μ_O. The oxygen chemical potentials μ_O used to evaluate the formation energy depends on the excess chemical potential, $\Delta\mu_O$, as $\mu_0 = (1/2)\mu_{O_2}(\text{molecule}) + \Delta\mu_o$. The $\Delta\mu_o$ varies according to the growth condition from 0 for oxygen-rich conditions to the minimum of the enthalpy of formation, $H_F/3$ (−6.19 eV/) of TSO, and $H_F/3$ (−4.86 eV) of KTO for oxygen-poor condition. Thus, ΔH of oxygen vacancy is lower in oxygen-poor conditions ($\Delta\mu_o \ll 0$) and higher in oxygen-rich conditions ($\Delta\mu_o \approx 0$).

For typical growth conditions of 2×10^{-6} torr pressure and 1023 K temperature, the value of $\Delta\mu_o$ is −2.036 eV. From the evaluated oxygen formation energy in a finite slab at the oxygen-poor conditions, we find $N(V_O) = 4.87\times10^{12}\,\text{cm}^{-2}$. Assuming that oxygen vacancies are fully ionized, i.e., each vacancy provides two free electrons, the resulting maximum electron density of the 2DEG is about $9.74\times10^{12}\,\text{cm}^{-2}$. This value is consistent with the experimentally reported carrier concentration at oxide interfaces [19]. We note though that while this quantitative agreement between the 2DEG density calculated for a particular slab and the experimentally measured value is excellent, the most important and general result here is the lowering of the oxygen vacancy formation energy at the TSO/KTO intermixed interface due to the orthorhombic distortion-driven release of internal pressure.

The formation of the interfacial 2DEG induced by oxygen vacancies is evident from Fig. 3(c), which shows the calculated LDOS of the TSO/KTO heterostructure with oxygen vacancy at the energetically favorable position [Fig. 3(b)]. It is seen that the Fermi energy lies near the bottom of the conduction bands of KTO making the interface metallic. This metallicity is caused by the transfer of unbound electrons generated by oxygen vacancy to the Ta-5*d* states forming the conduction band minimum of KTO. The conduction bands of TSO lie higher in energy than the conduction bands of KTO, and thus the TSO layers remain insulating.

3. *Interfacial electronic structure*

Figure 4 shows the electronic band structure for $(TSO)_3/(KTO)_{3.5}/(TSO)_{2.5}$ heterostructure that has oxygen vacancies at the intermixed interface, along with the high symmetry points *X*, Γ, and *M* in the Brillouin zone near the Fermi level. As the band gap of KTO is lower than that of TSO, the bands near the Fermi energy level could be considered as derived from the conduction band of KTO. However, the band order and character are modified due to reduced symmetry, quantum confinement, intermixing, and defect-induced relaxation. Like in bulk KTO, the crystal field split t_{2g} bands of

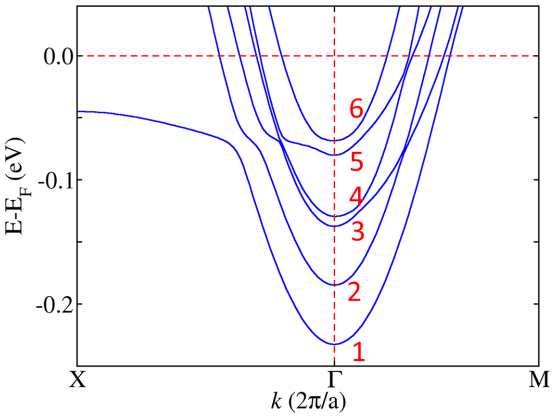

FIG. 4. Electronic band structure of the TSO/KTO/TSO oxygen vacant intermixed interface. The horizontal red line denotes the Fermi energy level, and the lowest five bands at the Γ points are labeled sequentially from 1 to 5.

Ta contribute mainly to the lower conduction bands; however, the bands are further split as symmetry is lowered. They also contain contributions from the t_{2g} bands of Sc as one of the Ta atoms at the interface is replaced by Sc. In Table II, we tabulate the orbital characters, ionic characters at the center of the Brillouin zone, Γ, and the effective mass of bands along two high symmetry directions, $\Gamma - X$ and $\Gamma - M$.

Out of the t_{2g} bands, the lower conduction bands crossing the Fermi energy level are contributed mainly by the in-plane d_{xy} states. Most out-of-plane t_{2g} bands generally lie higher in energy due to quantum confinement along the [001] direction. Out of six bands labeled in Fig. 4, only bands 4 and 6 have a significant contribution from the out-of-plane d_{xz} and d_{yz} orbitals because of distortion induced by the defect and intermixing. The lattice constant along the xand y directions at the interface deviates noticeably from that in bulk and that along the z direction.

TABLE II. Calculated effective mass for the conduction bands in TSO/KTO/TSO heterostructures having intermixed interface with oxygen vacancies in TSO and the orbital as well as ionic characteristics of bands at Γ point.

	Character Contributions (%)		$m*/m_e$	
Band	Orbital	Ionic	Γ-X	Γ-M
1	d_{xy} 91	Ta:Sc 87:8	0.49	0.47
2	d_{xy} 93	Ta:Sc 93:5	0.45	0.41
3	d_{xy} : d_{xz} 83:11	Ta:Sc 93:6	0.71	1.05
4	d_{xy} : d_{xz} 12:81	Ta:Sc 98:1	0.45	0.31
5	d_{xy} : d_{yz} 67:31	Ta:Sc 96:1	0.61	0.89
6	d_{xy} : d_{yz} 33:61	Ta:Sc 98:2	0.29	0.30
Average			0.5	0.57

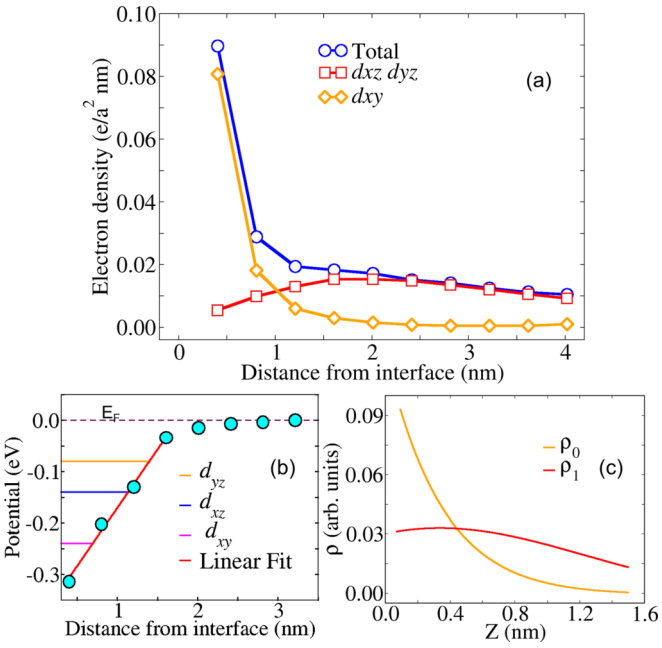

FIG. 5. Electron density (a) and potential energy (b) as a function of distance from the interface along with the KTO layers, for intermixed interface with oxygen vacancy, d_{xy}, d_{xz}, and d_{yz} indicate the energies of the corresponding orbitals with respect to Fermi energy. ρ_0 and ρ_1 in (c) are the probability density for first and second eigenfunctions obtained by solving 1D Schrodinger equation with the potential distribution.

The d_{xy} states near the bottom of conduction bands are split as the Ta atoms at different layers in the KTO face different potentials as shown in Fig. 5(b). The interfacial Ta faces the deepest potentials, with interfacial potential becoming shallower for layers away from the interface. The calculated interlayer potential difference between consecutive layers is as large as 0.1 eV [Fig. 5(c)]. Additionally, the Sc-3d states lie lower in energy compared to the Ta-5d states; as a result, the lower bands (1, 2, and 3) have a larger contribution from Sc compared to the higher bands (4, 5, and 6).

For evaluation of the effective mass, we fit each of the bands with a parabolic function and evaluate effective mass $m*$ as, $\frac{1}{m^*} = \frac{1}{\hbar^2}\frac{d^2E}{dk^2}$, where $\hbar$ is the reduced Planck constant, E is the energy, and k is the wave vector. Table II shows that the band with larger contributions from the in-plane Ta-d_{xy} orbitals has a smaller effective mass than those with larger contributions from the out-of-plane d_{yz} and d_{xz} orbitals. This is because the hopping matrix element, t, between the nearest neighbors is nonzero along both x and y directions for the in-plane d_{xy} orbitals. In contrast, t is nonzero only along the y and x directions for the d_{yz} and d_{xz} orbitals [51,52] as they protrude along the z direction. As a result, in the (001) heterostructure, the d_{xy} orbital has a larger bandwidth and a lower effective mass than d_{yz} and d_{xz} orbitals. Additionally, whenever the contribution of the Sc-3d band increases, the effective mass increases as 3d bands are heavier than 5d bands. Bands 1 and 2 have larger effective mass compared to band 6 despite the latter band having d_{yz} contribution. Band 6, which is purely of Ta-d_{xy}/d_{yz} is the lightest band among the six bands crossing the Fermi energy level, and it has an effective mass of 0.30 m_e.

The band structure, to a large extent, looks similar to other 2DEG systems despite different mechanisms for 2DEG generations: the lowest conduction band states are $dxy-$like, and d_{yz} and d_{xz} contribution increase for higher bands, and the average, the effective mass along Γ-X is smaller than the effective mass along Γ-M. The average value of the effective mass, 0.5 m_e (see Table II), is similar to the effective mass of a 3d-based 2DEG system such as LAO/STO [53,54].

4. Spatial distribution of 2DEG in KTO

To investigate the spatial distribution of 2DEG from the intermixed interface (with oxygen vacancy), we performed additional calculations by increasing the number of KTO layers to 15.5 uc (∼6 nm); the structure and LDOS are shown in Fig. S6. Figure 5(a) shows the calculated electron density as a function of distance from the interface. Each point in the plot represents the integrated local DOS up to the Fermi energy in a unit cell of KTO. The electron density is maximum at the KTO layer near the interface and decays away from about 2 nm from the interface.

The Ta-d suborbital resolved electronic density of state shows that the d_{xy} orbitals are strongly influenced by the deep potential well at the interface. It has a large density at the interface that decays exponentially as a function of distance and becomes negligible after 2 nm away from it. In contrast, the electron density due to d_{xz}/d_{yz} bands is smaller than d_{xy} near the interface, which first increases and then decreases as a function of distance from the interface. Other oxide interfaces [3,52,55,56] show a similar distribution of electron density with distance from the interface.

The different spatial distribution of electrons in d_{xy} and d_{xz}/d_{yz} orbitals leads to spatial-dependent transport. At or near the interface, transport is led by lighter, nearly free-electron-like d_{xy} electrons with a nearly circular free-electron-like Fermi surface Supplemental Material [35] S4), whereas far away from the interface, transport is led by heavier d_{xz}/d_{yz} electrons with an elliptical Fermi surface (Fig. S7). At the Lifshitz transition point [57,58], which lies at about 1 nm away from the interface, the transport behavior changes from that lead by d_{xy} to d_{xz}/d_{yz}. Around the Lifshitz transition point, competition between transport due to the d_{xy} and $d_{xy/yz}$ like electrons may lead to anomalous transport.

The interfacial charge distribution is determined by potential energy distribution at the KTO interface. Figure 5(b) shows the calculated potential energy, which increases linearly with distance at first, slows down (∼2 nm away from the interface) later, and finally becomes almost constant (∼3 nm away from the interface).

The spatial distribution of electronic charge from the interface is similar to the distribution of charge density of the lowest quantum states subjected to the potential. To demonstrate this, we numerically solve the one-dimensional Schrödinger equation, $-\frac{\hbar^2}{2m}\frac{d^2\psi_n}{dx^2} + V(z)\psi_n = E_n\psi_n$, where E_n are the eigenstates and ψ_n are corresponding eigenfunctions. Figure 5(c) shows the distribution of charge density, ρ_1 and ρ_2 calculated using the eigenfunctions, ψ_1 and ψ_2 of the two lowest eigenstates, which clearly shows similar behavior as d_{xy} and d_{yz}/d_{xz}.

The distribution of d_{xy} can also be explained using the probability density of the lowest eigenstate of 1D Schrodinger equation subjected to linear potential. The linear function, $V(x) = -V_0 + cx$, where V_0 is the minimum potential energy at the interface, and c is a constant that fits reasonably well to the evaluated potential distribution near the interface, as shown in Fig. 5(b). The analytical solutions to the 1D are the roots of Airy functions; see Supplemental Material [35] S5, and Refs. [59–61] therein. The probability density is then evaluated by $\rho_n = \int_0^{z_n} Ai(z)H(z_n)dz$, where $H(z_n)$ is a heavy sidestep function that is zero for $z < z_n$ and 1 for $z > z_n$. The probability density for the first eigenfunctions is shown in Supplemental Material [35] Fig. S8, which clearly shows similar behavior as d_{xy}.

IV. CONCLUSION AND OUTLOOK

We found that the polar-polar interface $(TbO)^+/(TaO_2)^+$ of the TSO/KTO is energetically unstable due to large Coulomb repulsion between two positively charged layers. So, this interface undergoes cation intermixing at the interface to alleviate the polar discontinuity resulting in an energetically stable interface. The density of states calculation shows that the intermixed interface is insulating. For the samples grown at low oxygen partial pressure, oxygen vacancies are likely to be formed. Our theoretical calculations show that oxygen vacancies are formed at the intermixed layer at the interface, making this interface metallic with a carrier density of about 10^{13} e/cm^2.

Our calculations clearly demonstrate that the interfacial two-dimensional electron gas in KTO/TSO interface is formed due to oxygen vacancies, unlike other interfaces in which 2DEG is formed due to polar discontinuity. The 2DEG occupies the Ta-5d bands that have an effective mass competitive with other 3d-based 2DEG systems such as LAO/STO [53,54]. The defect-induced 2DEG may provide opportunities for tuning 2DEG density in these interfaces.

ACKNOWLEDGEMENTS

This work was supported by a startup grant from the South Dakota School of Mines and Technology. T.R.P. acknowledges fruitful discussions with Dr. J. Lee, Dr. K. Eom and Professor C.-B. Eom. E.Y.T. acknowledges support from the National Science Foundation through the EPSCoR RII Track-1 program (NSF Award OIA-2044049). Computations were performed utilizing the Holland Computing Center at the University of Nebraska, Lincoln, and the Gamow Computing Cluster at the Department of Physics, South Dakota School of Mines and Technology.

[1] A. Ohtomo and H. Y. Hwang, A high-mobility electron gas at the $LaAlO_3/SrTiO_3$ heterointerface, Nature (London) **427**, 423 (2004).

[2] N. Nakagawa, H. Y. Hwang, and D. A. Muller, Why some interfaces cannot be sharp, Nat. Mater. **5**, 204 (2006).

[3] K. Song, S. Ryu, H. Lee, T. R. Paudel, C. T. Koch, B. Park, J. K. Lee, S.-Y. Choi, Y.-M. Kim, J. C. Kim, H. Y. Jeong, M. S. Rzchowski, E. Y. Tsymbal, C.-B. Eom, and S. H. Oh, Direct imaging of the electron liquid at oxide interfaces, Nat. Nanotechnol. **13**, 198 (2018).

[4] L. Qiao, T. C. Droubay, V. Shutthanandan, Z. Zhu, P. V. Sushko, and S. A. Chambers, Thermodynamic instability at the stoichiometric $LaAlO_3/SrTiO_3$ (001) interface, J. Phys.: Condens. Matter **22**, 312201 (2010).

[5] P. R. Willmott, S. A. Pauli, R. Herger, C. M. Schlepütz, D. Martoccia, B. D. Patterson, B. Delley, R. Clarke, D. Kumah, C. Cionca, and Y. Yacoby, Structural Basis for the Conducting Interface between $LaAlO_3$ and $SrTiO_3$, Phys. Rev. Lett. **99**, 155502 (2007).

[6] N. Pavlenko, T. Kopp, E. Y. Tsymbal, J. Mannhart, and G. A. Sawatzky, Oxygen vacancies at titanate interfaces: Two-dimensional magnetism and orbital reconstruction, Phys. Rev. B **86**, 064431 (2012).

[7] N. Pavlenko, T. Kopp, E. Y. Tsymbal, G. A. Sawatzky, and J. Mannhart, Magnetic and superconducting phases at the $LaAlO_3/SrTiO_3$ interface: The role of interfacial Ti 3d electrons, Phys. Rev. B **85**, 020407(R) (2012).

[8] C. Cen, S. Thiel, G. Hammerl, C. W. Schneider, K. E. Andersen, C. S. Hellberg, J. Mannhart, and J. Levy, Nanoscale control of an interfacial metal-insulator transition at room temperature, Nat. Mater. **7**, 298 (2008).

[9] G. Herranz, M. Basletić, M. Bibes, C. Carrétéro, E. Tafra, E. Jacquet, K. Bouzehouane, C. Deranlot, A. Hamzić, J.-M. Broto, A. Barthélémy, and A. Fert, High Mobility in $LaAlO_3/SrTiO_3$ Heterostructures: Origin, Dimensionality, and Perspectives, Phys. Rev. Lett. **98**, 216803 (2007).

[10] W. Siemons, G. Koster, H. Yamamoto, W. A. Harrison, G. Lucovsky, T. H. Geballe, D. H. A. Blank, and M. R. Beasley, Origin of Charge Density at $LaAlO_3$ on $SrTiO_3$ Heterointerfaces: Possibility of Intrinsic Doping, Phys. Rev. Lett. **98**, 196802 (2007).

[11] A. Kalabukhov, R. Gunnarsson, J. Börjesson, E. Olsson, T. Claeson, and D. Winkler, Effect of oxygen vacancies in the $SrTiO_3$ substrate on the electrical properties of the $LaAlO_3$, Phys. Rev. B **75**, 121404(R) (2007).

[12] Z. Zhong, P. X. Xu, and P. J. Kelly, Polarity-induced oxygen vacancies at $LaAlO_3/SrTiO_3$ interfaces, Phys. Rev. B **82**, 165127 (2010).

[13] M. Takizawa, S. Tsuda, T. Susaki, H. Y. Hwang, and A. Fujimori, Electronic charges and electric potential at $LaAlO_3/SrTiO_3$ interfaces studied by core-level photoemission spectroscopy, Phys. Rev. B **84**, 245124 (2011).

[14] N. C. Bristowe, P. B. Littlewood, and E. Artacho, Surface defects and conduction in polar oxide heterostructures, Phys. Rev. B **83**, 205405 (2011).

[15] W. A. Harrison, E. A. Kraut, J. R. Waldrop, and R. W. Grant, Polar heterojunction interfaces, Phys. Rev. B **18**, 4402 (1978).

[16] E. A. Kraut, Polar heterojunction interfaces: Isovalent interlayers, Phys. Rev. B **31**, 6875 (1985).

[17] T. Nakayama, Electronic structures of heterovalent (001) Semiconductor superlattices: GaP/ZnS and GaAs/ZnSe, J. Phys. Soc. Jpn. **61**, 2458 (1992).

[18] Y. Sun, Y. Liu, S. Hong, Z. Chen, M. Zhang, and Y. Xie, Critical Thickness in Superconducting $LaAlO_3/KTaO_3$ (111) Heterostructures, Phys. Rev. Lett. **127**, 086804 (2021).

[19] H. Zhang, H. Zhang, X. Yan, X. Zhang, Q. Zhang, J. Zhang, F. Han, L. Gu, B. Liu, Y. Chen, B. Shen, and J. Sun, Highly mobile two-dimensional electron gases with a strong gating effect at the amorphous $LaAlO_3/KTaO_3$ interface, ACS Appl. Mater. Interfaces **9**, 36456 (2017).

[20] N. Wadehra, R. Tomar, R. M. Varma, R. K. Gopal, Y. Singh, S. Dattagupta, and S. Chakraverty, Planar Hall effect and anisotropic magnetoresistance in polar-polar interface of $LaVO_3$-$KTaO_3$ with strong spin-orbit coupling, Nat. Commun. **11**, 874 (2020).

[21] S. Goyal, N. Wadehra, and S. Chakraverty, Tuning the electrical state of 2DEG at $LaVO_3$-$KTaO_3$ interface: Effect of light and electrostatic gate, Adv. Mater. Interfaces **7**, 1 (2020).

[22] Q. Song, R. Peng, H. Xu, and D. Feng, The spatial distribution of two-dimensional electron gas at the $LaTiO_3/KTaO_3$ interface, J. Phys.: Condens. Matter **29**, 315001 (2017).

[23] K. Zou, S. Ismail-Beigi, K. Kisslinger, X. Shen, D. Su, F. J. Walker, and C. H. Ahn, $LaTiO_3/KTaO_3$ interfaces: A new two-dimensional electron gas system, APL Mater. **3**, 036104 (2015).

[24] A. H. Al-Tawhid, D. P. Kumah, and K. Ahadi, Two-dimensional electron systems and interfacial coupling in $LaCrO_3/KTaO_3$ heterostructures, Appl. Phys. Lett. **118**, 1 (2021).

[25] S. Ryu, H. Zhou, T. R. Paudel, N. Campbell, J. Podkaminer, C. W. Bark, T. Hernandez, D. D. Fong, Y. Zhang, L. Xie, X. Q. Pan, E. Y. Tsymbal, M. S. Rzchowski, and C. B. Eom, Electronic reconstruction at the polar (111)-oriented oxide interface, APL Mater. **10**, 031115 (2022).

[26] J. Thompson, J. Hwang, J. Nichols, J. G. Connell, S. Stemmer, and S. S. A. Seo, Alleviating polarity-conflict at the heterointerfaces of $KTaO_3/GdScO_3$ polar complex-oxides, Appl. Phys. Lett. **105**, 102901 (2014).

[27] C. B. Eom (private communication, 2022).

[28] S. K. Ojha, S. K. Gogoi, P. Mandal, S. D. Kaushik, J. W. Freeland, M. Jain, and S. Middey, Oxygen vacancy induced electronic structure modification of $KTaO_3$, Phys. Rev. B **103**, 085120 (2021).

[29] G. Kresse and J. Furthmüller, Efficient Iterative Schemes for Ab Initio Total-Energy Calculations Using a Plane-Wave Basis Set, Phys. Rev. B **54**, 11169 (1996).

[30] G. Kresse and D. Joubert, From ultrasoft pseudopotentials to the projector augmented-wave method, Phys. Rev. B **59**, 1758 (1999).

[31] P. E. Blöchl, Projector augmented-wave method, Phys. Rev. B **50**, 17953 (1994).

[32] J. P. Perdew, K. Burke, and M. Ernzerhof, Generalized Gradient Approximation Made Simple, Phys. Rev. Lett. **77**, 3865 (1996).

[33] F. Karsch, A. Patkós, and P. Petreczky, Screened perturbation theory, Phys. Lett. B **401**, 69 (1997).

[34] X. Gonze, First-principles responses of solids to atomic displacements and homogeneous electric fields: Implementation of a conjugate-gradient algorithm, Phys. Rev. B **55**, 10337 (1997).

[35] See Supplemental Materials at http://link.aps.org/supplemental/10.1103/PhysRevMaterials.7.026201 which shows DOS of other considered interfaces and thicker superlattices, oxygen vacancy induced interfacial deformations, Fermi surface evolution, and analysis of electron charge density distribution.

[36] I. Petousis, D. Mrdjenovich, E. Ballouz, M. Liu, D. Winston, W. Chen, T. Graf, T. D. Schladt, K. A. Persson, and F. B. Prinz, High-throughput screening of inorganic compounds for

the discovery of novel dielectric and optical materials, Sci. Data **4**, 160134 (2017).

[37] S. Cabuk, H. Akkus, and A. M. Mamedov, Electronic and optical properties of $KTaO_3$: *Ab initio* calculation, Phys. B **394**, 81 (2007).

[38] B. Himmetoglu and A. Janotti, Transport properties of $KTaO_3$ from first-principles, J. Phys.: Condens. Matter **28**, 065502 (2016).

[39] Y. Fujii and T. Sakudo, Dielectric and optical properties of $KTaO_3$, J. Phys. Soc. Jpn. **41**, 888 (1976).

[40] S. Coh, T. Heeg, J. H. Haeni, M. D. Biegalski, J. Lettieri, L. F. Edge, K. E. O'Brien, M. Bernhagen, P. Reiche, R. Uecker, S. Trolier-McKinstry, D. G. Schlom, and D. Vanderbilt, Si-Compatible candidates for high κ dielectrics with the Pbnm perovskite structure, Phys. Rev. B **82**, 064101 (2010).

[41] H. M. Christen, G. E. Jellison, I. Ohkubo, S. Huang, M. E. Reeves, E. Cicerrella, J. L. Freeouf, Y. Jia, and D. G. Schlom, Dielectric and optical properties of epitaxial rare-earth scandate films and their crystallization behavior, Appl. Phys. Lett. **88**, 262906 (2006).

[42] S. H. Wemple, Some transport properties of oxygen-deficient single-crystal potassium tantalate ($KTaO_3$), Phys. Rev. **137**, A1575 (1965).

[43] G. E. Jellison, Jr, I. Pauluskas, L. A. Boatner, and D. J. Singh, Optical functions of $KTaO_3$ as determined by spectroscopic ellipsometry and comparison with band structure calculations, Phys. Rev. B **74**, 155130 (2006).

[44] H. Nakamura and T. Kimura, Electric field tuning of spin-orbit coupling in $KTaO_3$ field-effect transistors, Phys. Rev. B **80**, 121308(R) (2009).

[45] P. D. C. King, R. H. He, T. Eknapakul, P. Buaphet, S.-K. Mo, Y. Kaneko, S. Harashima, Y. Hikita, M. S. Bahramy, C. Bell, Z. Hussain, Y. Tokura, Z.-X. Shen, H. Y. Hwang, F. Baumberger, and W. Meevasana, Subband Structure of a Two-Dimensional Electron Gas Formed at the Polar Surface of the Strong Spin-Orbit Perovskite $KTaO_3$, Phys. Rev. Lett. **108**, 117602 (2012).

[46] K. V. Shanavas and S. Satpathy, Electric Field Tuning of the Rashba Effect in the Polar Perovskite Structures, Phys. Rev. Lett. **112**, 086802 (2014).

[47] J. P. Perdew and A. Zunger, Self-interaction correction to density-functional approximations for many-electron systems, Phys. Rev. B **23**, 5048 (1981).

[48] D. J. Singh, Stability and phonons of $KTaO_3$, Phys. Rev. B **53**, 176 (1996).

[49] C. Derks, K. Kuepper, M. Raekers, A. V. Postnikov, R. Uecker, W. L. Yang, and M. Neumann, Band-gap variation $InRScO_3$ (R = Pr, Nd, Sm, Eu, Gd, Tb, and Dy): X-ray absorption and O K-edge x-ray emission spectroscopies, Phys. Rev. B **86**, 155124 (2012).

[50] M. A. Moram, C. S. Ghedia, D. V. S. Rao, J. S. Barnard, Y. Zhang, M. J. Kappers, and C. J. Humphreys, On the origin of threading dislocations in GaN films, J. Appl. Phys. **106**, 073513 (2009).

[51] W. A. Harrison, *Electronic Structure and the Properties of Solids The Physics of the Chemical Bond* (Dover Publications, San Francisco, 1980).

[52] P. Larson, Z. S. Popović, and S. Satpathy, Lattice relaxation effects on the interface electron states in the perovskite oxide heterostructures: $LaTiO_3$ monolayer embedded in $SrTiO_3$, Phys. Rev. B Phys. **77**, 245122 (2008).

[53] V. R. Cooper, Enhanced carrier mobilities in two-dimensional electron gases at III-III/I-V oxide heterostructure interfaces, Phys. Rev. B **85**, 235109 (2012).

[54] W. Meevasana, P. D. C. King, R. H. He, S. K. Mo, M. Hashimoto, A. Tamai, P. Songsiriritthigul, F. Baumberger, and Z. X. Shen, Creation and control of a two-dimensional electron liquid at the bare $SrTiO_3$ surface, Nat. Mater. **10**, 114 (2011).

[55] Y. J. Chang, L. Moreschini, A. Bostwick, G. A. Gaines, Y. S. Kim, A. L. Walter, B. Freelon, A. Tebano, K. Horn, and E. Rotenberg, Layer-by-Layer Evolution of a Two-Dimensional Electron Gas Near an Oxide Interface, Phys. Rev. Lett. **111**, 126401 (2013).

[56] Z. S. Popović, S. Satpathy, and R. M. Martin, Origin of the Two-Dimensional Electron Gas Carrier Density at the $LaAlO_3/SrTiO_3$ Interface, Phys. Rev. Lett. **101**, 256801 (2008).

[57] S. Beaulieu, S. Dong, N. Tancogne-Dejean, M. Dendzik, T. Pincelli, J. Maklar, R. P. Xian, M. A. Sentef, M. Wolf, A. Rubio, L. Rettig, and R. Ernstorfer, Ultrafast dynamical Lifshitz transition, Sci. Adv. **7**, 1 (2021).

[58] A. Joshua, S. Pecker, J. Ruhman, E. Altman, and S. Ilani, A universal critical density underlying the physics of electrons at the $LaAlO_3/SrTiO_3$ interface, Nat. Commun. **3**, 1129 (2012).

[59] J. A. Anaya-Contreras, A. Zúñiga-Segundo, and H. M. Moya-Cessa, Airy eigenstates and their relation to coordinate eigenstates, Results Phys. **31**, 104904 (2021).

[60] M. U. Ali, The schrodinger equation of linear potential solution specializing to the stark effects, Int. J. Sci. Res. **4**, 490 (2015).

[61] L. F. Matin, H. H. Bouzari, and F. Ahmadi, Solving schrodinger equation specializing to the stark effect in linear potential by the canonical function method, J. Theor. Appl. Phys. **8**, 140 (2014).